Resonant Inelastic X-Ray Scattering Determination of the Electronic Structure of Oxyhemoglobin and Its Model Complex

James J. Yan,[†] Thomas Kroll,[†,§] Michael L. Baker,[†] Samuel A. Wilson,[†] Richard Decreau,[†] Marcus Lundberg,[†,‡] Dimosthenis Sokaras,[§] Pieter Glatzel,[⍰] Britt Hedman*[,§], Keith O. Hodgson*[,†,§], Edward I. Solomon*[,†,§]

[†] Department of Chemistry, Stanford University, Stanford, California 94305, United States

[§] Stanford Synchrotron Radiation Lightsource, SLAC National Accelerator Laboratory, Stanford University, Menlo Park, California 94025, United States

[‡] Department of Chemistry - Ångström Laboratory, Uppsala University, SE-751 21 Uppsala, Sweden

[⍰] ESRF, BP 220, 38043 Grenoble, Cedex 9, France

Abstract: Hemoglobin and myoglobin are oxygen-binding proteins with S=0 heme $\{FeO_2\}^8$ active sites. The electronic structure of these sites has been the subject of much debate. This study utilizes Fe K-edge X-ray absorption spectroscopy (XAS) and 1s2p resonant inelastic X-ray scattering (RIXS) to study oxyhemoglobin and a related heme $\{FeO_2\}^8$ model compound, [(pfp)Fe(1-MeIm)(O_2)] (pfp = meso-tetra(α,α,α,α-o-pivalamido-phenyl)porphyrin, or TpivPP, 1-MeIm = 1-methylimidazole) ($pfpO_2$), which was previously analyzed using L-edge XAS. The K-edge XAS and RIXS data of $pfpO_2$ and oxyhemoglobin are compared with the data for low-spin Fe^{II} and Fe^{III} $[Fe(tpp)(Im)_2]^{0/+}$ (tpp = tetra-phenyl porphyrin) compounds, which serve as heme references. The X-ray data show that $pfpO_2$ is similar to Fe^{II}, while oxyhemoglobin is qualitatively similar to Fe^{III}, but with significant quantitative differences. DFT calculations show that the difference between $pfpO_2$ and oxyhemoglobin is due to a distal histidine H-bond to O_2 and the less hydrophobic environment in the protein, which lead to more backbonding into the O_2. A valence bond configuration interaction multiplet model is used to analyze the RIXS data and show that $pfpO_2$ is dominantly Fe^{II} with 6-8% Fe^{III} character, while oxyhemoglobin has a very mixed wavefunction that has 50-77% Fe^{III} character and a partially polarized Fe-O_2 π bond.

Significance: The electronic structure of the heme oxy-iron center in oxyhemoglobin and oxymyoglobin has been the subject of debate for decades. Various experimental and computational methods have been used to study this system, leading to conflicting conclusions. This study uses X-ray spectroscopy to directly probe the iron center in the highly delocalized oxyhemoglobin and its model compound to define the electronic structure and understand the differences between the protein and the model. This study settles a longstanding debate in bioinorganic chemistry and provides insight into heme iron-oxygen binding, the key first step in many biocatalytic processes.

The electronic structure of the active sites in oxyhemoglobin (HbO_2) and oxymyoglobin has been the subject of study and debate for decades. The iron oxygen-binding proteins contain an S=0 $\{FeO_2\}^8$ active site, denoting eight valence electrons delocalized among the Fe 3d and O_2 π^* orbitals in the Enemark-Feltham notation used for metal-NO complexes. (1) Three electronic structure models have been proposed by Pauling (low-spin Fe^{II} with singlet O_2), (2, 3) Weiss (low-spin Fe^{III} antiferromagnetically-coupled to doublet O_2^-), (4) and McClure, Harcourt, and Goddard (S=1 Fe^{II} antiferromagnetically-coupled to triplet O_2, also known as the "ozone" model). (5-8) Much computational work has been done, with all three models supported by different calculations. (9-13) However, there has been a dearth of experimental data to directly probe the electronic structure. In particular the intense porphyrin $\pi \rightarrow \pi^*$ transitions of heme complexes make it difficult to probe the highly covalent Fe with traditional spectroscopic methods. (14)

X-ray absorption spectroscopy (XAS) has emerged as a site-specific technique that provides a direct probe of the metal center. An analysis of the iron K pre-edge suggested that HbO_2 has an electronic structure similar to the Weiss model in solution, but that crystalline HbO_2 has an electronic structure more similar to the Pauling model. (15) Alternatively, a recent X-ray emission Kβ study suggested that the iron center has an S = 1 spin state, similar to the ozone model. (16) However, neither technique provides a quantitative analysis of the electronic structure of iron centers. In contrast, L-edge XAS measures the electric dipole-allowed metal $2p \rightarrow 3d$ transitions, and the integrated intensity is proportional to the total amount of metal 3d character in the valence orbitals. (17) This makes the technique powerful in studying highly covalent metal sites. Quantitative covalency information can be extracted

through modeling of the L-edge XAS spectra using a valence bond configuration interaction (VBCI) multiplet model. (18) This methodology has been applied to iron complexes to extract the differential orbital covalency (DOC), which allows for quantification of ligand σ and π donation (17, 19, 20) and metal π back-bonding, (21) including in heme models. (14)

L-edge XAS and the VBCI multiplet model were used in a study to analyze the S=0 $\{FeO_2\}^8$ heme model compound [(pfp)Fe(1-MeIm)(O_2)] (pfp = meso-tetra(α,α,α,α-o-pivalamido-phenyl)porphyrin, 1-MeIm = 1-methylimidazole) ($pfpO_2$). (22) That study determined that the $pfpO_2$ model compound had an electronic structure more similar to the Pauling model. The $pfpO_2$ compound has been seen as a good model for HbO_2, with similar vibrational (23-26) and Mössbauer spectra. (27-32) One major difference between the model complex and the protein is that the protein has a conserved histidine in the active site that can hydrogen-bond to the O_2. This hydrogen-bond has been calculated by Shaik, et al. to be important in modulating the electronic structure of oxymyoglobin, leading to a more polarized Weiss-like description. (9) It is therefore important to experimentally compare the $pfpO_2$ model compound with the HbO_2 protein.

One major limitation of iron L-edge XAS is that it occurs in the soft X-ray regime (~710 eV), which requires ultrahigh vacuum, which limits the measurement of protein or solution samples. To measure the protein samples, hard X-rays (~7100 eV), such as used for iron K-edge XAS, are required. However, “L-edge like” information can be obtained through 1s2p resonant inelastic X-ray scattering (RIXS). (33) 1s2p RIXS involves a two-step process, where a hard X-ray incident photon of energy Ω causes a 1s→3d transition, followed by 2p→1s decay, releasing a photon of energy ω. (34, 35) The resulting $2p^5 3d^{n+1}$ final state configuration is the same as for L-edge XAS, which can be simulated with the VBCI multiplet model to extract the DOC and provide a quantitative bonding description. (36) 1s2p RIXS is a complementary technique to L-edge XAS and the differences between L-edge XAS and 1s2p RIXS have been previously studied with several non-heme iron model compounds. (37)

A combined L-edge XAS and 1s2p RIXS methodology was developed and applied to study the bonding in ferrous and ferric cytochrome c. (38) This involved an initial analysis of heme model compounds that could be measured by both L-edge XAS and 1s2p RIXS, which allowed for calibration of the VBCI model between the two techniques. The 1s2p RIXS analysis of the model compound was then used to calibrate the 1s2p RIXS analysis of the protein system, where L-edge XAS data were unavailable. This methodology is applied in the present study, by first studying the 1s2p RIXS of $pfpO_2$, for which the L-edge XAS analysis has been done, and then using this model as a reference for the analysis of the 1s2p RIXS of HbO_2.

Results and Analysis

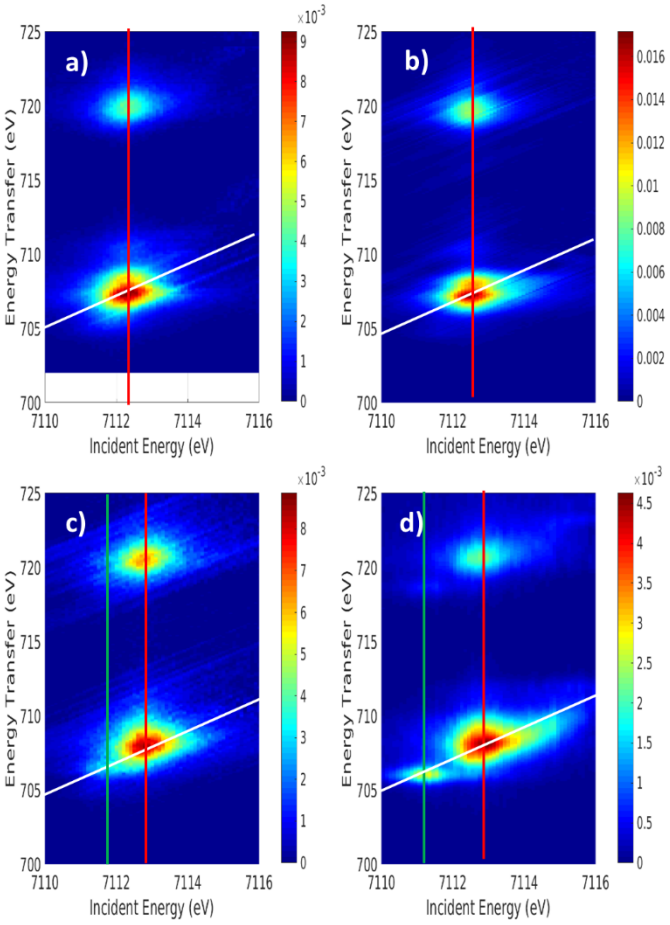

Figure 1: Background subtracted RIXS planes of (a) Fe2tpp, (b) $pfpO_2$, (c) HbO_2, and (d) Fe3tpp. The diagonal white lines represent where CEE cuts were made. The vertical red and green lines represent where CIE cuts were made.

RIXS Planes. The 2-dimensional background-subtracted RIXS data for both $pfpO_2$ and HbO_2 are shown in Figure 1b and 1c, respectively, along with the RIXS planes of $[Fe^{II}(tpp)(ImH)_2]$ (Fe2tpp, 1a) and $[Fe^{III}(tpp)(ImH)_2]^+$ (Fe3tpp, 1d) included as references for low-spin Fe^{II} and low-spin Fe^{III} in porphyrin environments (large version Figure S1). The RIXS planes for $pfpO_2$ and HbO_2 exhibit clear differences. The $pfpO_2$ plane has only a single incident energy resonance (x-axis) at 7112.2 eV. The main L_3 feature of the resonance is broad along the energy transfer direction (y-axis) and resolves into two peaks, with the main peak at 707.2 eV and an intense shoulder at 708.3 eV. At higher energy, a low-intensity satellite feature also appears at ~710 eV. The pattern of the RIXS plane of $pfpO_2$, with a single incident energy resonance and a double-peak feature in the energy transfer direction, is very similar to the pattern of the RIXS plane of Fe2tpp (Figure 1a).

Unlike $pfpO_2$, HbO_2 clearly shows two incident energy resonances, with a small, weak feature at 7111.4 eV, and a large, broad feature at 7112.8 eV. The 7112.8 eV resonance does not exhibit the double-peak feature seen in the $pfpO_2$ and Fe2tpp planes. The HbO_2 RIXS plane is not only different from the low-spin Fe^{II} reference plane, but is also very different from the low-spin Fe^{III} reference plane (Figure 1d). The "dπ"-resonance (7111.3 eV) in the Fe3tpp plane is higher in intensity than the low-energy resonance in HbO_2 and is also further separated in energy from the main peak (7112.9 eV) in the energy transfer direction. For Fe3tpp, the low-energy peak of the L_3 occurs at 706 eV in the energy transfer direction, with the main peak at 708 eV, compared to 706.5 eV and 708 eV, respectively in HbO_2. From the comparison of the RIXS planes, $pfpO_2$ experimentally appears very similar to Fe2tpp, while HbO_2 appears more "ferric-like" than $pfpO_2$, but significantly less than Fe3tpp.

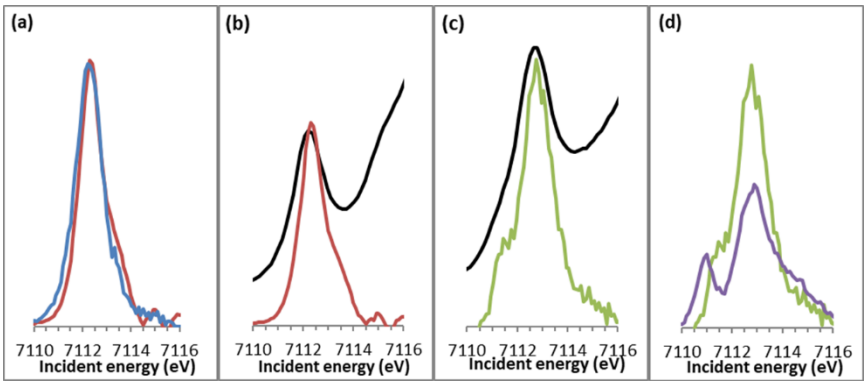

Figure 2: (a) Comparison of CEE cut of $pfpO_2$ (red) with Fe2tpp (blue). (b) Comparison of K-edge spectrum of $pfpO_2$ (black) with CEE cut (red). (c) Comparison of K-edge spectrum of HbO_2 (black) with CEE cut (green). (d) Comparison of CEE cut of HbO_2 (green) with Fe3tpp (purple).

CEE Cuts and K-edge Spectroscopy. The K-edge spectra of $pfpO_2$ and HbO_2 are shown in Figure 2b and c, along with comparisons to the corresponding constant emission energy (CEE) cuts (full K-edge XANES in Figure S2). The CEE cuts were made through the maxima of the RIXS planes and are marked by the diagonal white lines through the planes in Figure 1. The integrated intensity of the $pfpO_2$ pre-edge is 4.1 units, while the HbO_2 pre-edge is more intense at 6.7 units. The $pfpO_2$ pre-edge intensity is comparable to the pre-edge intensities of other six-coordinate low-spin ferrous and ferric compounds (3-5 units), (39) including Fe2tpp (4.9) and Fe3TPP (4.3). While HbO_2 has a more intense pre-edge than the other compounds, it is still significantly lower in intensity than the pre-edge intensities of distorted six-coordinate protein active sites (~8 units) (40) and of four-coordinate tetrahedral and square pyramidal five-coordinate compounds (11+ units). The latter have significant electric dipole intensity due to 4p-mixing caused by loss of inversion symmetry. (39) This means that the pre-edge features of $pfpO_2$ are primarily due to 1s→3d quadrupole excitations, but HbO_2 has a small amount of dipole intensity due to limited distortion at the Fe center.

In comparing the K-edges with the CEE cuts in Figure 2b and c, the main insight is that the CEE cuts in red and green provide a higher energy-resolution K-edge. In the CEE cut of $pfpO_2$, there is a single pre-edge peak, as in the K-edge, but with a higher energy shoulder. This shoulder is not due to a new 1s→3d excitation, but is due to overlap with the feature in the pre-edge that occurs at the same incident energy, but higher energy transfer in Figure 1b. This phenomenon was noted in our previous RIXS studies and emphasizes the need to collect the full 2-D RIXS plane in order to analyze these data. (37)

The high-resolution CEE cut of HbO_2 clearly shows two peaks, with a small peak at lower incident energy (Figure 2c). This peak is much less clear in the K-edge, where analysis of the second derivative is necessary to confirm the presence of the peak. The CEE cuts emphasize the differences between $pfpO_2$ and HbO_2 seen in the RIXS planes. To

compare cuts between the different samples, cuts were scaled such that the RIXS pre-edge integrated intensity was the same as that obtained through K-edge XAS. The $pfpO_2$ CEE cut is very similar to the CEE cut of Fe2tpp (Figure 2a). The HbO_2 CEE cut is very different from that of Fe3tpp (Figure 2d). While the lower-energy peak appears comparable in intensity to that in Fe3tpp, the energy splitting between the low-energy peak and the main peak is much smaller. The main peak in HbO_2 is also much more intense than in Fe3tpp. From the crystal structures of HbO_2, the Fe-O_2 bond length is ~1.8 Å, compared to ~2 Å for the other bonds. (41) This would lead to $4p_z$ mixing with d_{z2}, which would increase the intensity in the main peak. (39) Although HbO_2 displays two peaks in its CEE cut, it has significant and quantitative differences from the low-spin ferric reference spectrum.

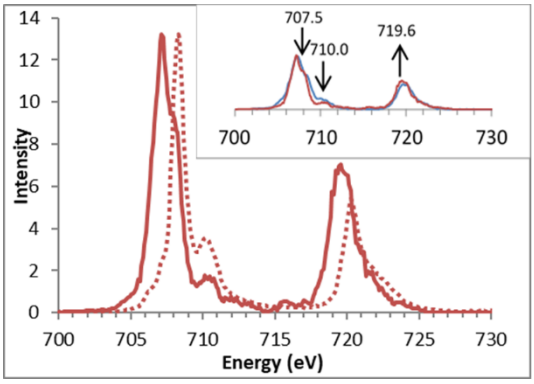

Figure 3: The CIE cut of $pfpO_2$ at 7112.2 eV (solid) with the L-edge spectrum (dotted). Inset: comparison of the CIE cut of $pfpO_2$ (red) with Fe2tpp (blue). Arrows show where $pfpO_2$ has different intensity from that of Fe2tpp.

CIE Cuts and L-edge Spectroscopy. The L-edge spectrum of $pfpO_2$ was analyzed in a previous study (22) and is compared with the constant incident energy (CIE) cut through the maximum of the RIXS pre-edge in Figure 3. The CIE is given by the red vertical lines in Figure 1. Unlike the L-edge spectrum (dotted), which has one prominent peak in the L_3 region, the CIE cut has a broad double-peak, with the lower-energy peak being higher in intensity. The higher energy satellite feature, at ~710 eV, is higher in intensity in the L-edge spectrum compared to the CIE cut. The L_2 region of the CIE cut is also higher in intensity compared with the L-edge spectrum. The inset in Figure 3 shows a comparison of the CIE cut of $pfpO_2$ with the CIE cut of Fe2tpp. The cuts are qualitatively very similar, with both showing a broad double-peak main feature in the L_3 region. There are however several notable differences between the two cuts, with the $pfpO_2$ cut having less intensity in the region at ~707.5 eV and in the higher energy satellite

feature at ~710 eV, but more intensity in the L_2 region (~720 eV), compared to the Fe2tpp cut. These differences are very similar to those previously observed comparing reduced cytochrome *c* to Fe2tpp, where there is also a change in the axial ligation (N to S). (38)

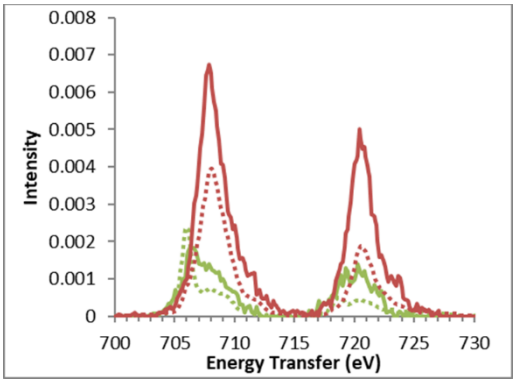

Figure 4: Comparison of CIE cuts of HbO_2 (solid) and Fe3tpp (dotted). CIE cuts through the low-energy peaks (at 7111.4 eV for HbO_2 and 7111.3 eV for Fe3tpp) are in green. CIE cuts through the main peaks (at 7112.8 eV for HbO_2 and 7112.9 eV for Fe3tpp) are in red. The CIE cuts are scaled to match the RIXS and K pre-edge integrated intensities.

For HbO_2, there is no comparison between L-edge and RIXS CIE cuts, due to the limitations in acquiring L-edge spectra on proteins. The comparison of the CIE cuts through the maxima of the two resonances in HbO_2 (given by the red vertical line in Fig. 1c) with the CIE cuts through the maxima of the two resonances in Fe3tpp is shown in Figure 4. The most significant difference between the two data sets comes from the CIE cut through the low-energy dπ peak (green). While the Fe3tpp cut (dotted) has a sharp, intense peak at 706 eV with some residual intensity from the main resonance at 708 eV, the HbO_2 cut (solid) has a lower intensity peak at 706.5 eV that is barely discernible from the residual intensity from the main resonance. In the CEE, the low energy peaks appear comparable in intensity, but the CIE cuts clearly show that the HbO_2 peak has lower intensity compared to Fe3tpp and has a smaller energy splitting between the low-energy peak and the main peak. The cuts through the main peak show similar shapes, but with HbO_2 having higher intensity due to the dipole contribution (vide supra).

Thus, the RIXS data show significant differences between HbO_2 and $pfpO_2$. $pfpO_2$ has spectral features qualitatively like that of the low-spin ferrous reference compound, while HbO_2 has two incident energy resonances, similar to that of the low-spin ferric reference compound. However, the HbO_2 spectrum has significant quantitative

differences in peak energy and intensity compared with the Fe3tpp spectrum. The next section uses DFT calculations to gain insight into the origin of these differences. The electronic structures of $pfpO_2$ and HbO_2 are analyzed further with VBCI modeling of these different RIXS planes in the last section of the analysis.

DFT Calculations. Based on the RIXS data, there are significant differences between the electronic structures of HbO_2 and $pfpO_2$. To understand the source of these differences, DFT calculations were performed on these systems using the crystal structures as the starting geometries, (41, 42) with toluene as the solvent in a polarized continuum model (PCM) for $pfpO_2$. For HbO_2, the proximal histidine, which binds directly to the Fe, as well as the distal histidine, which can H-bond with the O_2 and has been implicated in tuning the electronic structure of the site, (9) were included in the calculation as full amino acid residues (Figure S3). Additionally, a side chain carbonyl that may H-bond with the proximal histidine was modeled using a formaldehyde, (15) and a dielectric of 10 was used to model the protein environment. Geometry optimizations were performed on the starting structures using the BP86 functional. Parallel hybrid calculations with B3LYP gave similar results (Figure S4). In all cases, a polarized electronic structure was found lowest in energy by a few kcal/mol. Full computational details can be found in SI Materials and Methods.

Calculated % Metal 3d Character in Unoccupied Orbitals

Compound	σ (d_z^2)		σ ($d_{x^2-y^2}/_{xy}$)		π* (por)		π* (O_2)		Total[b]	Total Backbonding[c]	O_2 Backbonding
	α	β	α	β	α	β	α	β			
Fe2tpp	66.5	66.5	71.2	71.2	9.5	9.5	N/A	N/A	313.2 (302)	37.8	N/A
$pfpO_2$	63.2	55.5	68.6	64.1	9.5	2.9	59.8	9.0	344.9 (310)	93.5	68.8
HbO_2	61.3	56.7	68.1	63.6	6.1	2.3	64.4	11.8	342.7	93	76.2
Fe3tpp	66.5	63.3	67.2	62.8	5.7	2.1	70.9[a]	N/A	346.2 (365)	18.6	N/A

Table 1: Amount of metal 3d character in the lowest unoccupied orbitals calculated for the different compounds using the BP86 functional with experimental values in parentheses. For Fe2tpp, the closed shell solution was lowest in energy so α and β occupancies are the same. The metal values for the porphyrin π* orbitals are an average of two different orbitals. [a]This value for Fe3tpp represents the metal character in the dπ hole. [b]Experimental unoccupied 3d character comes from L-edge integrated intensity, which does not exist for HbO_2. [c]Total backbonding includes backbonding to both O_2 and porphyrin π* orbitals and is the sum of metal character from the orbitals.

The electronic structure results of the calculations are given in Tables 1 and S1 and Figure S5, along with calculations on Fe2tpp and Fe3tpp as reference compounds. The optimized structures of $pfpO_2$ and HbO_2 have very similar coordination environments around the Fe. The calculated electronic structures are also largely similar, with both having ~344% total unoccupied metal 3d character in the valence orbitals (Table 1). This is to be compared to 346% and 313% for the Fe3tpp and Fe2tpp references. Thus, both are calculated to be closer to Fe^{III}, however the experimental L-edge XAS total d character for $pfpO_2$ is closer to Fe^{II}. The main difference is found in the backbonding. While the total amount of backbonding of occupied Fe character into the porphyrin and O_2 π^* (Table 1) orbitals is the same for both complexes (~93%, Table 1), the distribution of this metal character is different. $pfpO_2$ has less backbonding into the O_2 π^* (68.8% vs 76.2%), which is compensated by increased backbonding into the porphyrin π^* orbitals. This difference in Fe-O_2 bonding explains the slightly longer Fe-O (1.83 vs 1.82 Å) and shorter O-O (1.30 vs 1.32 Å) calculated bonds in $pfpO_2$ compared to HbO_2 (Table S1).

Based on the models used for the calculation, this difference in backbonding can be due to several factors: 1) the carbonyl H-bond to the proximal histidine, 2) the dielectric, 3) the distal histidine H-bond to the O_2, and/or 4) the different porphyrins (heme b vs picket-fence porphyrin). These factors were investigated through perturbations to the HbO_2 model (Figure S6). Removing the carbonyl H-bond to the proximal histidine in the calculation showed minimal effect (76.2% vs 76.1% backbonding to O_2) on the electronic structure, in contrast to previous calculations. (15) Then lowering the dielectric constant from 10 (protein) to 2.4 (toluene) decreased the backbonding to O_2 from 76.1% to 74.3%, while subsequent removal of the distal histidine further lowered the backbonding to 69.1%, similar to $pfpO_2$. The latter effect has been described by Shaik et al. (9) Since this perturbed heme b model has the same bonding description as in pfp, these calculations show that this difference in porphyrin has minimal effect on the electronic structure; the primary effect coming from the distal histidine H-bond to O_2, and the less hydrophobic environment of the protein pocket.

The difference in backbonding to the O_2 qualitatively explains the spectral differences between $pfpO_2$ and HbO_2 in the RIXS data. As seen in the VBCI modeling (vide infra), increased backbonding from the Fe into the O_2 leads to a more polarized electronic structure associated with the appearance of the low energy feature seen in the HbO_2 RIXS plane. In comparing the $pfpO_2$ and HbO_2 calculations with those of Fe2tpp and Fe3tpp, both are more like Fe3tpp than Fe2tpp (Figure S5, right and left, respectively). The π-bonding into O_2 leads to a low-energy α hole with significant metal character (~63%), like the dπ hole in Fe3tpp (70.9%) (purple orbital α1 in Figure S5). The total unoccupied metal 3d character is also very close to that of Fe3tpp (346.2%), but not Fe2tpp (313.2%). This significantly contrasts the experimental XAS and RIXS data, which show that $pfpO_2$ is more like Fe2tpp, and that HbO_2, while having a pre-edge feature associated with spin polarization, is still significantly different from Fe3tpp (vide supra). TD-DFT calculations were also performed, which also show that the HbO_2 and $pfpO_2$ calculations are more ferric-like than seen experimentally (see SI TD-DFT Analysis).

VBCI Modeling. Since the DFT calculations provide a spin-polarized electronic structure description for both $pfpO_2$ and HbO_2 that have more ferric character than the experimental data suggest, a semi-empirical VBCI multiplet model was used to fit the RIXS data to lock in on the electronic structure of the two compounds. The VBCI model can provide a quantitative measure of the DOC in a metal complex through mixing the ground $3d^n$ configuration with ligand-to-metal charge transfer (LMCT) ($3d^{n+1}\underline{L}$, $\underline{L}$ = ligand hole) and metal-to-ligand charge transfer (MLCT) ($3d^{n-1}\underline{L}^-$) configurations, respectively. The weight of the configurations in the mixed wavefunction depends on the relative energy of the configurations and the strength of the mixing.

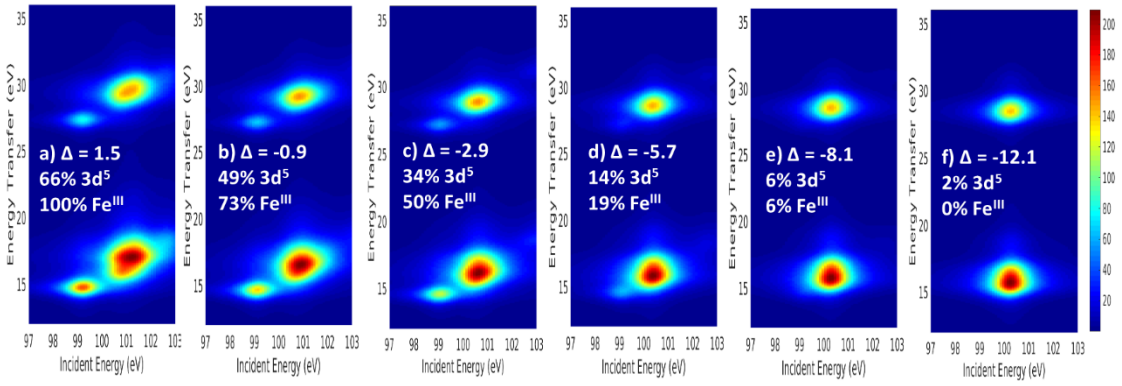

Figure 5: VBCI RIXS simulations progressing from $Fe^{III} \rightarrow Fe^{II}$ using the ferric $3d^5$ ground configuration, starting with the fit for Fe3tpp in a, with fits for HbO_2 (c), $pfpO_2$ (e), and Fe2tpp (f). Full fit parameters for Fe3tpp can be found in Table S2. In this series, Δ is decreased from 1.5 in a, to -12.1 in f, decreasing the weight of the $3d^5$ configuration and becoming dominantly $3d^6$.

Previous studies have shown that by varying the weights of the charge transfer configurations, it is possible to simulate ferrous (and ferric) L-edge spectra using both a ferric and a ferrous ground configuration. (21, 22) This approach can be applied to 1s2p RIXS simulations as well. Figure 5 shows a series of RIXS simulations, starting with the low-spin ferric simulation of Fe3tpp on the left (a). In the Fe3tpp simulation, the energy difference between the LMCT ($3d^6$) configuration and the ground ($3d^5$) configuration, Δ, is 1.5 eV. As Δ decreases, the weight of the LMCT configuration increases and the wavefunction gains more ferrous character, becoming 3% $3d^5$ in the rightmost simulation (f). The low energy dπ peak also decreases in intensity and shifts up in energy, eventually merging into the main peak in Figure 5e.

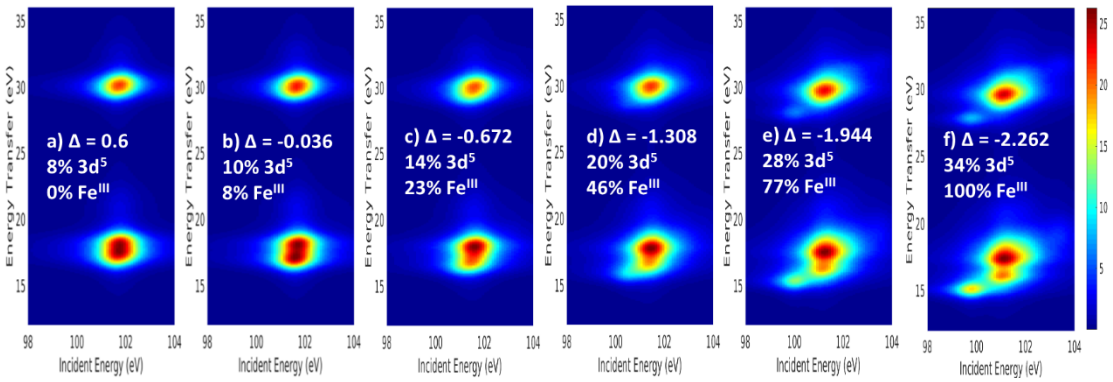

Figure 6: VBCI RIXS simulations progressing from $Fe^{II} \rightarrow Fe^{III}$ using the ferrous $3d^6$ ground configuration, starting with the fit for Fe2tpp in a, with fits for $pfpO_2$ (b), HbO_2 (e), and Fe3tpp (f). Full fit parameters for Fe2tpp can be found in Table S2. In this series, Δ_{bb} is decreased from 0.6 in a, to -2.262 in f.

Figure 6 shows a series of RIXS simulations, starting with the low-spin ferrous simulation of Fe2tpp on the left. In this series, the energy difference between the MLCT ($3d^5$) and ground ($3d^6$) configurations, Δ_{bb}, is decreased going from left to right. As the weight of the MLCT configuration increases, the wavefunction gains more ferric character, and a low-energy dπ peak appears in Figure 6d, which gains in intensity and moves to lower energy. Correlation of these

simulations to the HbO_2 data, which has a low-intensity dπ peak close in energy to the main peak (Figures 1 and 2), show that they can be simulated as a mixed wavefunction of low-spin $3d^6$ and $3d^5$ configurations; thus qualitatively it can either be described as a low-spin ferric site with strong π donation into the dπ hole, or a low-spin ferrous center with extensive π backbonding into the O_2.

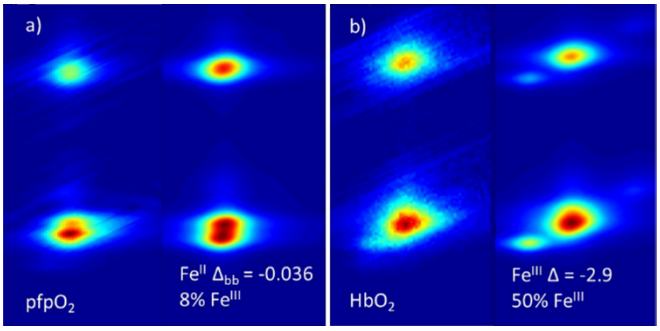

Figure 7: Best VBCI fits from the simulations described in Figures 5 and 6 for a) $pfpO_2$ and b) HbO2 with the experimental data on the left, and the fit on the right. Since the results showed that $pfpO_2$ is dominantly Fe^{II}, the Fe^{II} fit is given. In the case of HbO_2, the results showed a mixed wavefunction that is more Fe^{III}, and therefore the Fe^{III} fit is given. For HbO_2, the experimental data contains dipole character in the main peak, while the simulation only contains quadrupole character. Therefore, the best fit was based on the energy splitting of the low-energy peak from the main peak and the relative intensity of the low-energy peak compared to the Fe3tpp fits, rather than the intensity ratio of the low-energy peak to the main peak.

By fitting the Fe2tpp, $pfpO_2$, HbO_2, and Fe3tpp data along the Fe^{III}→Fe^{II} (Figure 5) and Fe^{II}→Fe^{III} (Figure 6) series, the amount of Fe^{II}/Fe^{III} character in each system can be estimated to obtain a more quantitative description of the electronic structure. The simulated integrated CEE and CIE were compared with the experimental data to find the best match within a series (Figures S7 and S8, Table S3). Since the VBCI model only calculates quadrupole intensity, it is directly comparable to the $pfpO_2$, Fe2tpp, and Fe3tpp data sets. However, because the HbO_2 contains some dipole intensity in the main peak, the intensity and energy splitting of the low energy peak is the primary handle for comparing the VBCI simulations to the experimental data. The Fe2tpp and Fe3tpp fits were used as Fe^{II} and Fe^{III} limits, (38) representing 0% and 100% "Fe^{III}" character, respectively. The first limit corresponds to 2% $3d^5$ character and the second limit to 66% $3d^5$ character. The difference between Fe^{III} and $3d^5$ character comes from ligand donation and backdonation present already in the reference complexes. The Fe^{III} character for $pfpO_2$ and HbO_2 were then defined relative to those references (SI VBCI Fitting). The resulting fits (Figure 7) show that along the Fe^{III}→Fe^{II} series, $pfpO_2$ has 6% Fe^{III} character, while HbO_2 has 50% Fe^{III} character. In the Fe^{II}→Fe^{III} series,

$pfpO_2$ has 8% Fe^{III} character, while HbO_2 has 77% Fe^{III} character. Thus, the fitting shows that $pfpO_2$ is dominantly Fe^{II}, and that HbO_2 has a very mixed Fe^{II}/Fe^{III} wavefunction that has more Fe^{III} character.

Discussion

From the VBCI modeling of the 1s2p RIXS data, HbO_2 is best described as a polarized mixed Fe^{II}/Fe^{III} system that has 50-77% Fe^{III} character. This contrasts with $pfpO_2$, which is best described as an unpolarized Fe^{II} with 6-8% Fe^{III} character. The modeling also shows that the difference in electronic structure can be attributed to the covalency of the Fe-O_2 π bond. HbO_2 has significantly more Fe^{III} character than $pfpO_2$ because of greater π backbonding to O_2. While DFT calculations give a more "Fe^{III}" description for $pfpO_2$ and HbO_2 than is found experimentally, they do qualitatively reproduce the difference in O_2 backbonding, which is due to the distal histidine H-bond to the O_2 combined with the less hydrophobic protein environment. Both are important in polarizing the Fe-O_2 π bond. In previous studies on {FeNO}[6], it was found that the degree of polarization is governed by the magnitude of the energy gap of the Fe-NO π bonding and antibonding orbitals relative to the strength of the exchange interaction between electrons in these orbitals. (43) When the energy gap is large relative to the exchange interaction, the bond remains unpolarized. As the energy gap decreases, the wavefunction becomes more polarized (Scheme S1). $pfpO_2$ thus has a large enough energy gap to result in an unpolarized bonding description. The addition of the H-bond and increased dielectric in the protein stabilize the O_2 π* orbital energy, which leads to polarization of the Fe-O_2 π bond and the appearance of a low-energy peak in the RIXS spectrum in Fig. 1c.

These electronic structure descriptions, unpolarized Fe^{II} for $pfpO_2$ and mixed Fe^{II}/Fe^{III} for HbO_2 due to greater π backbonding into O_2 are reasonably consistent with other experimental data. L-edge XAS provided evidence that $pfpO_2$ is an unpolarized Fe^{II} with moderate backbonding to O_2. (22) The K-edge of HbO_2 is shifted slightly higher in energy compared to $pfpO_2$ (Figure S2), and both are between Fe2tpp and Fe3tpp, with $pfpO_2$ closer to Fe2tpp and HbO2 closer to Fe3tpp. Although previous iron Kβ measurements on HbO_2 and oxymyoglobin suggested the iron is S = 1 based on the high intensity of a satellite peak at ~7045 eV, we have measured the Kβ spectrum of the HbO_2

sample used here (characterized as being 3% met by EPR) and found a significantly weaker satellite feature that is not consistent with an S = 1 Fe (Figure 11). (16) The Fe^{II} S = 1 description of HbO_2 also requires polarized Fe-O π backbonding and polarized O-Fe σ donation. Attempts to use the VBCI multiplet model to simulate the experimental RIXS data using this description were unsuccessful. The RIXS analysis is also consistent with previous vibrational and Mössbauer spectroscopic studies (see SI Discussion on $\{FeO_2\}^8$ O-O Stretching Frequencies and Mössbauer Parameters).

These results also provide an experimental basis for further calculations. As observed in the previous section, DFT calculations provide a poor description of these oxy-Fe sites. DFT is a single determinant method and gives ferric descriptions, while the data indicate more ferrous character. Multi reference methods, such as CASSCF are best to correlate to these data. Importantly, the experimental data show the H-bond and protein environment have a large effect on the $\{FeO_2\}^8$ electronic structure, inducing some polarization in the Fe-O_2 π bond. While some calculations have considered these effects and predicted a more polarized bond, (9, 12) other computational studies do not take these factors into account. These RIXS data on the electronic structure of oxyhemoglobin and its pfp model should provide the experimental basis for more detailed electronic structure considerations.

Materials and Methods

Oxy-picket-fence porphyrin samples were prepared as described in ref. 30. Hemoglobin samples were prepared as described in ref. 15. K-edge XAS data were collected at beam line 7-3 at the Stanford Synchrotron Radiation Lightsource (SSRL). RIXS data were collected at beam line 6-2 at SSRL and ID-26 at the European Synchrotron Radiation Facility (ESRF). VBCI modeling was performed using the models developed by Cowan (44) and Thole et al. (45) DFT calculations were performed using the Orca 3.0.3 software package. (46) Full details on sample preparation, spectroscopic experiments, and calculations are included in SI Materials and Methods.

Acknowledgements: This work was supported by the National Institutes of Health (GM-40392 to E.I.S.). Use of the Stanford Synchrotron Radiation Lightsource, SLAC National Accelerator Laboratory, is supported by the U.S. Department of Energy, Office of Science, Office of Basic Energy Sciences under Contract No. DE-AC02-76SF00515. The SSRL Structural Molecular Biology Program is supported by the DOE Office of Biological and Environmental Research, and by the National Institutes of Health, National Institute of General Medical Sciences (P41GM103393 to K.O.H and B.H.). T.K. acknowledges financial support by the German Research Foundation (DFG) grant KR3611/2-1. M.L.B. acknowledges the support of the Human Frontier Science Program.

References:

1. Enemark JH & Feltham RD (1974) Principles of structure, bonding, and reactivity for metal nitrosyl complexes. *Coordination Chemistry Reviews* 13(4):339-406.
2. Pauling L & Coryell CD (1936) The Magnetic Properties and Structure of Hemoglobin, Oxyhemoglobin and Carbonmonoxyhemoglobin. *Proceedings of the National Academy of Sciences* 22(4):210-216.
3. Pauling L (1964) Nature of the Iron-Oxygen Bond in Oxyhaemoglobin. *Nature* 203(4941):182-183.
4. Weiss JJ (1964) Nature of the Iron-Oxygen Bond in Oxyhaemoglobin. *Nature* 202(4927):83-84.
5. McClure DS (1960) Electronic Structure of Transition-Metal Complex Ions. *Radiation Research Supplement* 2:218-242.
6. Harcourt RD (1971) Increased-valence formulae and the bonding of oxygen to haemoglobin. *International Journal of Quantum Chemistry* 5(5):479-495.
7. Harcourt RD (1990) Comment on a CASSCF study of the Fe-O_2 bond in a dioxygen heme complex. *Chemical Physics Letters* 167(4):374-377.
8. Goddard WA & Olafson BD (1975) Ozone Model for Bonding of an O_2 to Heme in Oxyhemoglobin. *Proceedings of the National Academy of Sciences* 72(6):2335-2339.
9. Chen H, Ikeda-Saito M, & Shaik S (2008) Nature of the Fe–O_2 Bonding in Oxy-Myoglobin: Effect of the Protein. *J. Am. Chem. Soc.* 130(44):14778-14790.
10. Liao M-S, Huang M-J, & Watts JD (2010) Iron Porphyrins with Different Imidazole Ligands. A Theoretical Comparative Study. *The Journal of Physical Chemistry A* 114(35):9554-9569.
11. Attia AAA, Lupan A, & Silaghi-Dumitrescu R (2013) Spin state preference and bond formation/cleavage barriers in ferrous-dioxygen heme adducts: remarkable dependence on methodology. *RSC Advances* 3(48):26194-26204.
12. Kepp KP & Dasmeh P (2013) Effect of Distal Interactions on O_2 Binding to Heme. *The Journal of Physical Chemistry B* 117(14):3755-3770.
13. Jensen KP & Ryde U (2004) How O_2 Binds to Heme: REASONS FOR RAPID BINDING AND SPIN INVERSION. *Journal of Biological Chemistry* 279(15):14561-14569.
14. Hocking RK*, et al.* (2007) Fe L-Edge X-ray Absorption Spectroscopy of Low-Spin Heme Relative to Non-heme Fe Complexes:? Delocalization of Fe d-Electrons into the Porphyrin Ligand. *J. Am. Chem. Soc.* 129(1):113-125.

15. Wilson SA*, et al.* (2013) X-ray absorption spectroscopic investigation of the electronic structure differences in solution and crystalline oxyhemoglobin. *Proc. Natl. Acad. Sci.* 110(41):16333-16338.
16. Schuth N*, et al.* (2017) Effective intermediate-spin iron in O_2-transporting heme proteins. *Proc. Natl. Acad. Sci.* 114(32):8556-8561.
17. Wasinger EC, de Groot FMF, Hedman B, Hodgson KO, & Solomon EI (2003) L-edge X-ray Absorption Spectroscopy of Non-Heme Iron Sites: Experimental Determination of Differential Orbital Covalency. *J. Am. Chem. Soc.* 125(42):12894-12906.
18. Baker ML*, et al.* (2017) K- and L-edge X-ray absorption spectroscopy (XAS) and resonant inelastic X-ray scattering (RIXS) determination of differential orbital covalency (DOC) of transition metal sites. *Coordination Chemistry Reviews* 345:182-208.
19. Hocking RK*, et al.* (2009) Fe L- and K-edge XAS of Low-Spin Ferric Corrole: Bonding and Reactivity Relative to Low-Spin Ferric Porphyrin. *Inorg. Chem.* 48(4):1678-1688.
20. Hocking RK*, et al.* (2010) Fe L-Edge X-ray Absorption Spectroscopy Determination of Differential Orbital Covalency of Siderophore Model Compounds: Electronic Structure Contributions to High Stability Constants. *J. Am. Chem. Soc.* 132(11):4006-4015.
21. Hocking RK*, et al.* (2006) Fe L-Edge XAS Studies of $K_4[Fe(CN)_6]$ and $K_3[Fe(CN)_6]$: A Direct Probe of Back-Bonding. *J. Am. Chem. Soc.* 128(32):10442-10451.
22. Wilson SA*, et al.* (2013) Iron L-Edge X-ray Absorption Spectroscopy of Oxy-Picket Fence Porphyrin: Experimental Insight into Fe–O_2 Bonding. *J. Am. Chem. Soc.* 135(3):1124-1136.
23. Barlow CH, Maxwell JC, Wallace WJ, & Caughey WS (1973) Elucidation of the mode of binding of oxygen to iron in oxyhemoglobin by infrared spectroscopy. *Biochemical and Biophysical Research Communications* 55(1):91-95.
24. Maxwell JC, Volpe JA, Barlow CH, & Caughey WS (1974) Infrared evidence for the mode of binding of oxygen to iron of myoglobin from heart muscle. *Biochemical and Biophysical Research Communications* 58(1):166-171.
25. Potter WT, Tucker MP, Houtchens RA, & Caughey WS (1987) Oxygen infrared spectra of oxyhemoglobins and oxymyoglobins. Evidence of two major liganded oxygen structures. *Biochemistry* 26(15):4699-4707.
26. Collman JP, Brauman JI, Halbert TR, & Suslick KS (1976) Nature of O_2 and CO binding to metalloporphyrins and heme proteins. *Proceedings of the National Academy of Sciences* 73(10):3333-3337.
27. Tsai TE, Groves JL, & Wu CS (1981) Electronic structure of iron‐dioxygen bond in oxy‐Hb‐A and its isolated oxy‐α and oxy‐β chains. *The Journal of Chemical Physics* 74(8):4306-4314.
28. Boso B, Debrunner PG, Wagner GC, & Inubushi T (1984) High-field, variable-temperature mössbauer effect measurement on oxyhemeproteins. *Biochimica et Biophysica Acta (BBA) - Protein Structure and Molecular Enzymology* 791(2):244-251.
29. Oshtrakh MI*, et al.* (2011) Heme iron state in various oxyhemoglobins probed using Mössbauer spectroscopy with a high velocity resolution. *BioMetals* 24(3):501-512.
30. Spartalian K, Lang G, Collman JP, Gagne RR, & Reed CA (1975) Mössbauer spectroscopy of hemoglobin model compounds: Evidence for conformational excitation. *The Journal of Chemical Physics* 63(12):5375-5382.
31. Collman JP*, et al.* (1980) Synthesis and characterization of "tailed picket fence" porphyrins. *Journal of the American Chemical Society* 102(12):4182-4192.
32. Li J, Noll BC, Oliver AG, Schulz CE, & Scheidt WR (2013) Correlated Ligand Dynamics in Oxyiron Picket Fence Porphyrins: Structural and Mössbauer Investigations. *Journal of the American Chemical Society* 135(41):15627-15641.
33. Glatzel P & Bergmann U (2005) High resolution 1s core hole X-ray spectroscopy in 3d transition metal complexes—electronic and structural information. *Coord. Chem. Rev.* 249(1–2):65-95.
34. Glatzel P*, et al.* (2004) The Electronic Structure of Mn in Oxides, Coordination Complexes, and the Oxygen-Evolving Complex of Photosystem II Studied by Resonant Inelastic X-ray Scattering. *J. Am. Chem. Soc.* 126(32):9946-9959.

35. de Groot FMF*, et al.* (2005) 1s2p Resonant Inelastic X-ray Scattering of Iron Oxides. *J. Phys. Chem. B* 109(44):20751-20762.
36. Kroll T, Lundberg M, & Solomon EI (2016) X-Ray Absorption and RIXS on Coordination Complexes. *X-Ray Absorption and X-Ray Emission Spectroscopy*, (John Wiley & Sons, Ltd), pp 407-435.
37. Lundberg M*, et al.* (2013) Metal–Ligand Covalency of Iron Complexes from High-Resolution Resonant Inelastic X-ray Scattering. *J. Am. Chem. Soc.* 135(45):17121-17134.
38. Kroll T*, et al.* (2014) Resonant Inelastic X-ray Scattering on Ferrous and Ferric Bis-imidazole Porphyrin and Cytochrome c: Nature and Role of the Axial Methionine–Fe Bond. *J. Am. Chem. Soc.* 136(52):18087-18099.
39. Westre TE*, et al.* (1997) A Multiplet Analysis of Fe K-Edge 1s → 3d Pre-Edge Features of Iron Complexes. *J. Am. Chem. Soc.* 119(27):6297-6314.
40. Wasinger EC*, et al.* (2002) X-ray Absorption Spectroscopic Investigation of the Resting Ferrous and Cosubstrate-Bound Active Sites of Phenylalanine Hydroxylase. *Biochemistry* 41(20):6211-6217.
41. Park S-Y, Yokoyama T, Shibayama N, Shiro Y, & Tame JRH (2006) 1.25 Å Resolution Crystal Structures of Human Haemoglobin in the Oxy, Deoxy and Carbonmonoxy Forms. *Journal of Molecular Biology* 360(3):690-701.
42. Jameson GB*, et al.* (1978) Structure of a dioxygen adduct of (1-methylimidazole)-meso-tetrakis(α, α, α, α,,-o-pivalamidophenyl)porphinatoiron(II). An iron dioxygen model for the heme component of oxymyoglobin. *Inorg. Chem.* 17(4):850-857.
43. Yan JJ*, et al.* (2017) L-Edge X-ray Absorption Spectroscopic Investigation of $\{FeNO\}^6$: Delocalization vs Antiferromagnetic Coupling. *J. Am. Chem. Soc.* 139(3):1215-1225.
44. Cowan RD (1981) *The theory of atomic structure and spectra* (University of California Press, Berkeley) pp xviii, 731 p.
45. Thole BT*, et al.* (1985) 3d X-ray-absorption lines and the $3d^9 4f^{n+1}$ multiplets of the lanthanides. *Phys. Rev. B* 32(8):5107-5118.
46. Frank N (2012) The ORCA program system. *Wiley Interdisciplinary Reviews: Computational Molecular Science* 2(1):73-78.